SUPPLEMENTARY INFORMATION

Supplement A: System parameters and operating points

The device is a one-dimensional array of capacitvely coupled transmon qubits, employed in our previous work in [1, 2]. Each transmon has a tunable resonance frequency in the range $\omega_{01}/2\pi \approx (4-6)$ GHz, with on-site interactions set by their anharmonicity $U/2\pi \approx 240$ MHz. The transmon qubits are frequency-tunable by terminating them with a superconducting quantum interference device (SQUID) loop that is inductively coupled to its individual current bias line used for threading magnetic flux through the loop. The capacitive coupling between nearest-neighbor transmon sites sets a tunneling rate of $J/2\pi \approx 9$ MHz. For site-resolved readout, each qubit is capacitively coupled to a $\lambda/2$ coplanar waveguide (CPW) resonator. The readout resonators are evenly staggered between $\omega_R/2\pi \approx (7-8)$ GHz, with linewidths $\kappa_R/2\pi \approx 100$ kHz and qubit-resonator dispersive couplings in the range $\chi_{qR}/2\pi \approx (0.5-1.6)$ MHz. The readout resonators are individually coupled to their own $\lambda/2$ CPW Purcell resonators (filters) that are all coupled to a common CPW feedline. The feedline allows us to send all qubit drive pulses (when the qubits are resolved at different frequencies) and perform frequency multiplexed readout, while the Purcell filters reduces the effect of qubit decay (T_1 relaxation) into the feedline environment.

In this paper we use different frequency configurations for the transmon qubits, both ordered and disordered, to operate and probe our synthetic material. The experiments involve tuning the qubits between these frequency configurations, diabatically or adiabatically, as detailed in section SI D. The configurations are the following:

- **large disorder staggered configuration**: In this configuration the qubits are staggered in a zig-zag frequency pattern, where neighboring qubits are detuned by $> U$ and next-to-nearest neighbors are detuned by $> 2J$. In this stagger we initialize the localized photons and the ancilla state with microwave pulses and perform site-resolved dispersive readout of qubit populations.

- **small disorder staggered configuration**: In this configuration we prepare the localized photons prior to the adiabatic evolution to the ordered lattice. The qubit frequencies are staggered such that the qubits on the left of the ancilla are at higher frequencies than the qubit on the right side. The seven-qubit N00N state is prepared over all sites $Q_0 - Q_6$ and we use Q_3 as the ancilla. The five-qubit N00N state is prepared over a subset of the site $Q_2 - Q_6$ and we use Q_4 as the ancilla.

- **inverted small disorder staggered configuration**: This configuration is used in the inverted disorder protocol for preparing the N00N states described in Section III. After preparing the $|\text{solid}\rangle + |\text{fluid}\rangle$ in the ordered lattice, we prepare the N00N state in the disordered (computational) basis by adiabatically ramping the qubits to this inverted configuration where the qubits on the right of the ancilla are at a higher frequency than the qubits on the left side.

- **ordered transistor configuration**: In this configuration the sites are nearly degenerate at the lattice frequency, except for the ancilla qubit detuned that is detuned by U. In other words, the $\omega_{01}/2\pi$ frequency of the left and right qubits match the $\omega_{12}/2\pi$ ancilla frequency. In this transistor configuration, the transport of photons is conditioned on the quantum state of the ancilla as explained in Section III.

Qubit relaxation T_1 and decoherence T_2^* times are measured as a function of frequency to avoid low-lifetime regions coupled to TLS defects. We use these frequency scans to identify optimal staggered configurations and lattice frequencies. We also monitor T_1, T_2 over time and find average values $T_1 \approx 45$µs, $T_2 \approx 1.5$ µs. At the closely degenerate lattice configuration, we expect the qubit T_2's to be enhanced by the flux sweet-spots generated from the avoided crossings of the energy levels. To mitigate decoherence effects through the flux bias lines, where we are sending control signals at different bandwidths, we can consider incorporating on-chip stepped-impedance filters [3] in future designs.

The list of system parameters and operating points are detailed in Table I. These parameters were measured using standard experimental techniques in circuit QED, outlined in several modern reviews [4].

Supplement B: Ramsey interferometry measurements

The many-body Ramsey interferometry measurements are conducted following a procedure similar to our previous work in ref. [2]. In essence, it involves performing a Ramsey interference experiment on the ancilla qubit to extract its $|0\rangle \to |1\rangle$ transition frequency ω_{01} relative to the frequency tone ω_d used for driving the ancilla. First, the ancilla qubit is prepared in a superposition $\frac{1}{\sqrt{2}}(|0\rangle + |1\rangle)$ with a microwave $\pi/2$ pulse. After a hold time Δt, the two superposition states develop a relative phase $\Delta\phi = (\omega_{01} - \omega_d)\Delta t$. Varying the hold time leads to oscillations around the equator of

Qubit	**0**	**1**	**2**	**3**	**4**	**5**	**6**
$U_{\text{lattice}}/2\pi$ (MHz)	-241	-240	-240	-231	-234	-239	-240
$J_{i,i+1}/2\pi$ (MHz)	9.062	9.032	8.842	8.936	9.023	9.040	–
$\omega_{\text{large-disorder}}/2\pi - 5310$ (MHz)	215	-265	262	-205	309	-308	357
$\omega_{\text{small-disorder}}/2\pi - 5310$ (MHz) (5 qubit protocol)	–	–	50	100	234	-100	-50
$\omega_{\text{transistor-config}}/2\pi - 5310$ (MHz) (5 qubit protocol)	–	–	0	0	234	0	0
$\omega_{\text{inverted-disorder}}/2\pi - 5310$ (MHz) (5 qubit protocol)	–	–	-50	-100	234	100	50
$\omega_{\text{small-disorder}}/2\pi - 5310$ (MHz) (7 qubit protocol)	75	125	100	231	0	0	0
$\omega_{\text{transistor-config}}/2\pi - 5310$ (MHz) (7 qubit protocol)	0	0	0	231	0	0	0
$\omega_{\text{transistor-config}}/2\pi - 5310$ (MHz) (7 qubit protocol)	0	0	0	231	-100	-125	-75
$T1(\mu s)$	14.6	35.5	57.7	28.4	60.3	54.7	40.0
$T2^*(\mu s)$	0.85	0.64	1.31	0.77	3.57	0.84	1.4
single-shot readout fidelity	0.91	0.92	0.93	0.95	0.87	0.92	0.83
$\omega_{\text{read}}/2\pi$ (GHz)	6.197	6.323	6.427	6.556	6.655	6.78	6.871
$\kappa_{\text{read}}/2\pi$ (kHz)	359	553	203	235	292	220	894
$\chi_{\text{rd-qb}}/2\pi$ (MHz)	0.48	1.23	0.78	1.24	0.90	1.71	0.73

Table I. **System Parameters**

the Bloch sphere, which we can convert to oscillations in qubit population with a second $\pi/2$ pulse. From the fringe oscillations in the measured ancilla occupation $P_{|1\rangle} = \frac{1}{2}(1 + \cos\Delta\phi)$, we extract the qubit frequency ω_{01}.

When applying the quantum-controlled transport protocol for creating N00N states, the ancilla becomes entangled with the other qubits in the lattice during the hold time in the Ramsey sequence. This leads to an enhancement in the accrued relative phase $\Delta\phi = (\omega_{01} + \Delta_{MB} - \omega_d)\Delta t$, registered as an increase in the fringe frequency equal to the energy difference between the qubit frequencies $\Delta_{MB} = \omega_R - \omega_L$ on the right and left of the ancilla.

The time resolution of the Analog-to-Digital Converter (ADC) used for measuring the ancilla occupation is 1 ns, which sets a bandwidth limit of 500 MHz for recording the Ramsey fringe frequency without aliasing. We record a large number of fringe periods within a fraction of the decoherence time budget by setting a frequency difference $(\omega_{01} - \omega_d)/2\pi \simeq 50$ MHz. Detuning the drive frequency by 50 MHz from the ancilla transition would significantly reduce the amplitude contrast of the Ramsey fringes. Instead, we incorporate a time-dependent virtual phase to our second $\pi/2$ pulse in the Ramsey sequence to virtually change the reference frequency of the qubit drive. As shown in Fig. 2c, we record the Ramsey fringes for 200 ns in steps of 1 ns, leading to a frequency resolution of 5 MHz.

Supplement C: Flux Control and Crosstalk

1. Flux control

This experiment relies on the precise and fast control of the transmon qubit frequencies that set the energy landscape of the lattice. The on-site qubit frequencies are tuned by applying currents to dedicated flux bias lines inductively coupled to each transmon SQUID.

There are two types of flux control signals used in this experiment. DC flux bias currents are used for statically tuning the qubit frequencies to a target staggered (disordered) configuration for performing readout and single-qubit microwave control (for injecting photons and changing readout basis). Fast RF flux bias pulses are used for providing additional dynamic frequency tuning (on top of the static disordered configuration) to perform our many-body operations at ns (diabatic control) and µs (adiabatic control) time-scales. The DC and RF flux bias signals are combined with bias tees, anchored to the mixing chamber stage, and routed to each individual flux bias line.

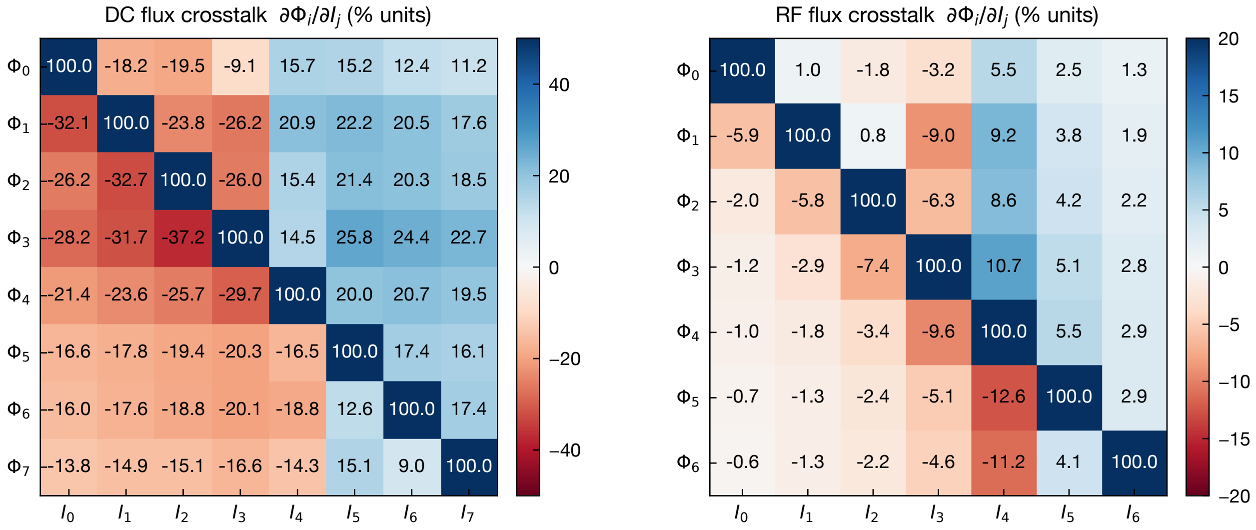

	I_0	I_1	I_2	I_3	I_4	I_5	I_6	I_7
Φ_0	100.0	-18.2	-19.5	-9.1	15.7	15.2	12.4	11.2
Φ_1	-32.1	100.0	-23.8	-26.2	20.9	22.2	20.5	17.6
Φ_2	-26.2	-32.7	100.0	-26.0	15.4	21.4	20.3	18.5
Φ_3	-28.2	-31.7	-37.2	100.0	14.5	25.8	24.4	22.7
Φ_4	-21.4	-23.6	-25.7	-29.7	100.0	20.0	20.7	19.5
Φ_5	-16.6	-17.8	-19.4	-20.3	-16.5	100.0	17.4	16.1
Φ_6	-16.0	-17.6	-18.8	-20.1	-18.8	12.6	100.0	17.4
Φ_7	-13.8	-14.9	-15.1	-16.6	-14.3	15.1	9.0	100.0

	I_0	I_1	I_2	I_3	I_4	I_5	I_6
Φ_0	100.0	1.0	-1.8	-3.2	5.5	2.5	1.3
Φ_1	-5.9	100.0	0.8	-9.0	9.2	3.8	1.9
Φ_2	-2.0	-5.8	100.0	-6.3	8.6	4.2	2.2
Φ_3	-1.2	-2.9	-7.4	100.0	10.7	5.1	2.8
Φ_4	-1.0	-1.8	-3.4	-9.6	100.0	5.5	2.9
Φ_5	-0.7	-1.3	-2.4	-5.1	-12.6	100.0	2.9
Φ_6	-0.6	-1.3	-2.2	-4.6	-11.2	4.1	100.0

Supplemental Information Fig. S1. **DC and RF Flux Crosstalk Matrices**

In addition to the on-chip flux bias lines, a solenoid of superconducting niobium-titanium (NbTi) wire is attached (and thermally anchored) to the device package to provide a global magnetic field for arranging the qubit frequencies close to the target staggered configuration. This helps greatly reduce the static DC currents applied to the on-chip bias lines and minimize heating effects.

2. DC and RF Crosstalk

In our device there is non-negligible cross-talk between the flux bias lines. We need to characterize and calibrate this crosstalk between all qubits and bias lines (at different timescales) to have independent control over each qubit frequency. The amount of flux Φ_i threading the SQUID loop for a given transmon Q_i is affected not only by its dedicated bias current I_i, but also by the currents $I_{j\neq i}$ in all other flux bias lines.

We assume that any set of flux bias values $\vec{\Phi} = \mathbf{M}\vec{I}$ is linearly dependent on the applied currents $\vec{I}$ through the crosstalk matrix $\mathbf{M}$, where the total flux response if given by $d\Phi_i = \sum_{i=1}^{N} \frac{\partial\Phi_i}{\partial I_j} dI_j$. Each individual matrix element $M_{ij} = \partial\Phi_i/\partial I_j$ corresponds to the mutual inductive coupling between the SQUID loop i and flux control line j. We employ the same procedure as in [1, 5] for measuring the matrix elements M_{ij}. We bias qubit Q_i at a point in its flux dispersion where its frequency ω_i^0 is linearly sensitive to small changes in flux (or current). Using pump-probe qubit spectroscopy, we measure the slope $\partial\omega_i/\partial I_j$ from the variation in qubit frequency when separately varying each bias current I_j. The crosstalk matrix element is then calculated by dividing the measured slope by the diagonal variation of the qubit frequency ω_i with applied flux Φ_i, taking on the general formula $M_{ij} = (\partial\omega_i/\partial I_j)/(\partial\omega_i/\partial\Phi_i)|_{\omega_i^0}$. The qubit frequency to flux conversion is extracted by fitting the measured flux-dependent qubit dispersion $\omega_i = \omega_i(\Phi_i)$ to a Jaynes-Cummings model that takes into account the coupling to individual readout resonators. From the inverted linear dependence on crosstalk $\vec{I} = \mathbf{M}\vec{\Phi}$, the combination of bias currents I_j needed to independently tune each qubit frequency to any target $\omega_i(\Phi_i)$ is calculated from the eigenvectors of inverted crosstalk matrix M_{ij}^{-1}.

The measured crosstalk matrix for static dc flux control is shown in SI Fig. S1, where the rows are normalized to the diagonal elements to display the relative magnitude of the off-diagonal crosstalk elements. The fast RF flux crosstalk matrix is also shown in SI Fig. S1, measured from the step response of 10 µs long square pulses with a 1 ns rise time. We observe minimal drifts ($< 0.2\%$) in the measured DC and RF crosstalk matrices between different cooldowns of the same device and control line configurations.

3. Disorder and Pulse Corrections

The precision of qubit frequency tuning is limited by the accuracy of our measured crosstalk matrices, flux dispersion $\omega_i(\Phi)$, and cancellation of flux pulse distortions. Using the DC crosstalk matrix, we can reach target frequencies in the staggered configuration to within $\delta\omega_{01}/2\pi \lesssim 10$ MHz. After additional rounds of dispersion corrections $\omega_i(\Phi)$, we reduce the discrepancy to $\delta\omega_{01}/2\pi \lesssim 100$ kHz. Using the RF crosstalk matrix, we can dynamically hit the intended on-site frequencies for our near-degenerate lattice experiments to within $\delta\omega_{01}/2\pi \lesssim 2$ MHz. By measuring the density profiles of our photon fluids at the near-degenerate lattice configuration, and comparing it to theory, we can compensate for additional on-site disorder to further reduce it to $\delta\omega_{01}/2\pi \lesssim 100$ kHz.

In addition to the crosstalk calibrations, the precision in the real-time control of the qubit frequencies (lattice potential) relies on also correcting distortions in the short-time response of the fast RF flux lines. The flux control pulses, used for both diabatic (≈ 1ns) and adiabatic (≈ 100ns) control, are distorted by the low-pass filters on the RF line. We probe this distortion in spectroscopy by measuring the qubit frequency in response to a flux step pulse and perform a similar kernel correction to the work done in [1, 5].

Supplement D: Pulse Sequences

The typical pulse sequences used for the conditional transport and many-body interferometry experiments are illustrated in SI Fig. S2. All experiments start with the qubits, in their ground state, DC flux-biased at the large-disordered configuration, where neighboring qubits are detuned by $> U$ (defined in section SI A). At this staggered configuration we initialize the system with photons by sequentially applying microwave π-pulses to each frequency-resolved lattice site. We also initialize the ancilla qubit in $|0\rangle$, $|1\rangle$ or $(|0\rangle+|1\rangle)/\sqrt{2}$ using π or $\pi/2$ pulses. All microwave qubit pulses have Gaussian envelopes truncated at $\pm 2\sigma$.

Following the injection of photons in the disordered lattice, we rapidly (diabatically) tune the qubits to a smaller staggered configuration where the qubits on the left hand side of the aniclla are at higher frequencies than the ones on the right, and the ancilla qubit is frequency detuned by U from the target lattice frequency. The staggered frequency configurations used for seven and five qubit experiments are detailed in section SI A. The qubits are then adiabatically ramped to lattice degeneracy in the transistor configuration: the $\omega_{01}/2\pi$ frequency of the left and right qubits matches the $\omega_{12}/2\pi$ frequency of the ancilla. If the ancilla is prepared in the $|0\rangle$, $|1\rangle$ or $(|0\rangle + |1\rangle)/\sqrt{2}$ state, this adiabatic protocol leads to preparing a solid (Mott insulator), fluid (Tonks-Girardeau gas), or coherent superposition of both $|\text{solid}\rangle + |\text{fluid}\rangle$ in the ordered lattice. To probe these states, we freeze tunneling dynamics and onsite occupancy by rapidly (diabatically) tuning the qubits back to the large staggered disorder configuration and apply microwave pulses to each readout resonator to perform site-resolved qubit occupation measurements using heterodyne dispersive readout. For further details regarding the dispersive readout techniques employed for the transmon chain, see the supplemental section of our previous work [1].

For adiabatically ramping the qubit frequencies we use flux pulses with an exponential shape. This simple approach captures the natural process of the many-gap decreasing as the sites' energies are tuned closer to each other. The total time t_{ramp} of these exponential ramps varies with system size. The ramps we use have the functional form $\propto A_\Phi(1 - e^{-t/\tau})$ with the range of timescales $\tau \in \left[\frac{2}{5}t_{\text{ramp}}, \frac{3}{5}t_{\text{ramp}}\right]$. We optimize the values for the timescale τ and total ramp time t_{ramp}, dependent on the number of photons and lattice size, to satisfy adiabaticity by using the reversibility probe employed in our previous work [1].

Following the preparation of the $|\text{solid}\rangle + |\text{fluid}\rangle$ state, we can extend the sequence to prepare the N00N state in the disordered (computational) basis. In this work we explore two approaches:

- **inverted disorder protocol** (section III): we adiabatically re-introduce disorder and ramp the qubits to an inverted (*different*) disorder configuration, where the qubits on the right hand side of the ancilla have a higher frequency than the ones on the left (the ancilla qubit remains at the same frequency).
- **phonon assisted protocol** (section IV): we flux modulate one lattice site to generate particle-hole excitations (phonons) on the fluid component of the superposition to transfer occupation to the fluid state on the opposite edge of the hardcore band (more details in section SI E). We re-introduce disorder by ramping to qubits to the *same* staggered configuration we originally started with, where the qubits on the left hand side of the ancilla have a higher frequency.

With both of these approaches we prepare a N00N state corresponding to a superposition of photons localized on the left and right hand side of the ancilla. If we wish to probe this entangled state with our many-body Ramsey protocol, we let the system freely evolve at the current frequency stagger, for a hold time which we linearly vary over ~ 200 sequences, to accumulate a relative phase that encodes the information about our many-body state. Then we

Inverted disorder protocol

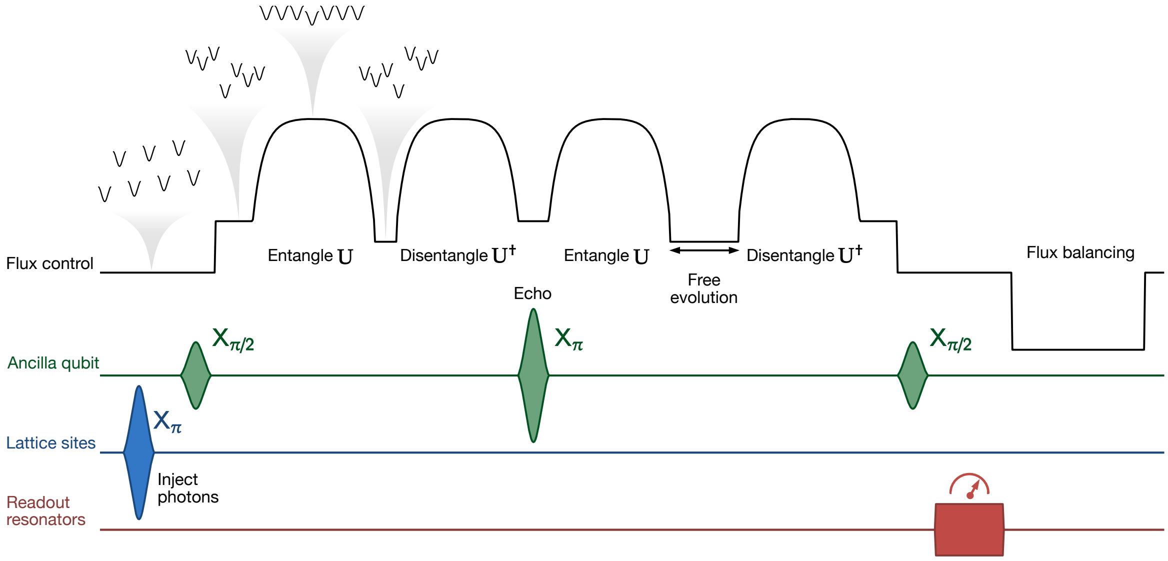

Phonon assisted protocol

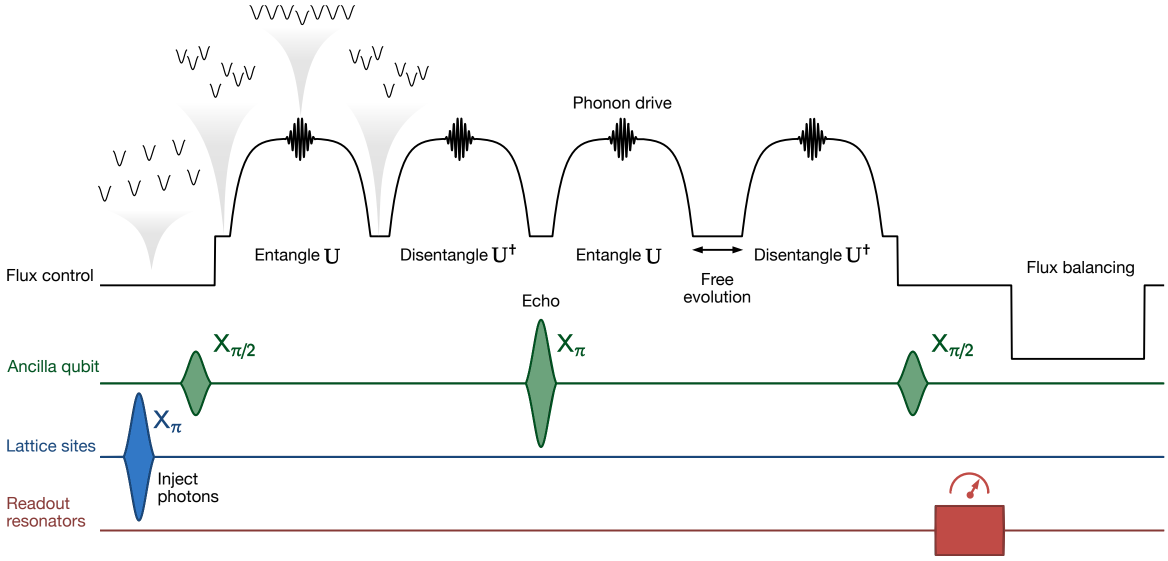

Supplemental Information Fig. S2. **Pulse sequence** for the drive and flux control pulses used in the two entangling protocols and their corresponding echo sequence

localize this phase information into the ancilla qubit by time-reversing the entanglement pulse sequence, involving two adiabatic ramps and an optional flux modulation tone if employing phonons. We then rapidly tune the qubits to the original large stagger and apply a second $\pi/2$ pulse on the ancilla qubit prior to the readout pulse to convert the oscillations around the equator (from varying the hold time) to fringe oscillations in the qubit occupation. More details are included in section SI B. This Ramsey sequence is adapted to measure the many-body echo in section V by applying a π pulse on the ancilla qubit in the middle of the Ramsey hold time.

The flux bias lines have stray inductances that lead to a very slow ($>$ 1ms) residual response to flux pulses that induces unwanted qubit frequency drifts. To counteract this effect, at the end of each experimental sequence (after the readout pulse) we apply a flux balancing pulse to cancel the net current flux within one experiment period.

The experiment pulse sequences are repeated every 500µs, allowing sufficient idling time for the qubits and readout resonators to decay to their ground state before the start of the next experiment sequence.

Supplement E: Phonon Transport

The key insight in section IV is the capability of performing quantum-controlled multi-qubit SWAP operations, and leveraging it for preparing N00N states, by exciting phonons in the ordered lattice. This can be intuitively understood from translating the description of the our 1D lattice of strongly interacting photons, described by the Bose-Hubbard Hamiltonian

$$\mathbf{H}_{\mathrm{BH}}/\hbar = J \sum_{\langle i,j \rangle} a_i^\dagger a_j + \frac{U}{2} \sum_i n_i \left(n_i - 1\right) + \sum_i \omega_{\mathrm{i}} n_i, \tag{S1}$$

in the hard-core limit, to a system of non-interacting fermions [6, 7]. To accomplish this, we define operators through a Jordan-Wigner transformation

$$f_i \triangleq \left[\prod_{j<i} (1 - 2a_j^\dagger a_j) \right] a_i \tag{S2}$$

which obey fermionic anticommutation relations $\{f_i, f_j\} = \delta_{ij}$. The Bose-Hubbard Hamiltonian then becomes a tight-binding model for non-interacting fermions

$$H = J \sum_{\langle i,j \rangle} f_i^\dagger f_j + \sum_i \omega_i f_i^\dagger f_i \tag{S3}$$

$$= \sum_k \varepsilon_k f_k^\dagger f_k \tag{S4}$$

written in diagonal form using the Fourier transformed fermionic operators $f_k = \frac{1}{\sqrt{N+1}} \sum_j e^{i \frac{\pi k}{N+1} j} f_j$. For a fermionic 1D lattice with N sites and open boundary conditions, the single-particle eigenenergies are $\varepsilon_k = 2J \cos(\frac{\pi k}{N+1})$, where $k \in \{1, N\}$ are the quasi-momenta.

This description is convenient when describing the many-body states in any M-particle ($M < N$) hardcore band, since by simply filling the single-particle fermion states, obeying the Pauli exclusion principle, one produces M-particle eigenstates $|\Psi_{k_1,k_2,\ldots,k_M}\rangle = f_{k_1}^\dagger f_{k_2}^\dagger \ldots f_{k_M}^\dagger |0\rangle$ with corresponding energies $E_{k_1,k_2,\ldots,k_M} = \sum_{k=k_1}^{k_M} \varepsilon_k$. The lowest $|\Psi_{\mathrm{min}}\rangle$ energy (ground) state simply corresponds to filling up the lowest energy single-particle states, up to the Fermi momentum $|k| < k_F$. The phonons correspond to collective modes (density oscillations) in the fluid that get excited as particle-hole pairs $f_{k+q}^\dagger f_k |\Psi_{\mathrm{min}}\rangle$ where one fermion state is taken from the occupied state $k < k_F$ (resulting in a vacant state k, i.e. a hole) and promoted to an occupied state above the Fermi level $k + q > k_F$. The phonon excitation caries a net momentum q, and the energy required to excite the mode, on top of the ground state energy, is $\varepsilon_{k+q} - \varepsilon_k$. Due to particle-hole symmetry in our system, the phonon analogy applies also when starting in the highest energy state in the hardcore band by filling up the M highest-energy single-particle fermion states. This becomes relevant as in our experiment we conditionally prepare the highest energy fluid state prior to applying phonon-induced SWAP operations.

For the experiment presented in section IV, we are looking at $M = 2$ particles in $N = 5$ sites. The multi-qubit SWAP operation involves transferring photons from the highest frequency transmons on the left side (Q_2, Q_3) to the lowest frequency one on the right side (Q_5, Q_6), conditioned on the quantum state of the middle ancilla qubit (Q_4). Our adiabatic control maps thesse localized two-photon states in the disordered lattice to the highest and lowest fluids states of the ordered lattice in the transistor configuration (Q_4 frequency ω_{01} detuned by U from the lattice frequency). In terms of fermion operators, the lowest and highest fluid states correspond to $|\Psi_{1,2}\rangle = b_1^\dagger b_2^\dagger |0\rangle$ and $|\Psi_{4,5}\rangle = b_4^\dagger b_5^\dagger |0\rangle$, respectively, where the indices denote the quasi-momentum states $\pi k/6$, $k \in \{1, 5\}$. The task of swapping photons between sites in the disordered configuration becomes the task of transferring excitations between the extreme fluid states in the hardcore band, which we realize through a two-phonon process $|\Psi_{1,2}\rangle = (b_1^\dagger b_4)(b_2^\dagger b_5)|\Psi_{4,5}\rangle$ that simultaneously creates two particle-hole pairs between the free fermion states $k = 1$ & $k = 4$ and $k = 2$ & $k = 5$.

We drive this two-phonon process by flux-modulating the transmon qubit Q_3 with a flat-top gaussian pulse applied through the RF fast-flux line. Since the frequency of the transmon is flux-tunable $\omega_{01} = \omega_{01}(\Phi)$, applying a flux modulation tone $\epsilon_\Phi \cos(\omega_d t)$ on top of the static bias Φ_{dc} leads to a modulation of the transmon frequency $\omega_{01}(\Phi_{\mathrm{dc}} + \epsilon_\Phi \cos(\omega_d t)) \approx \bar{\omega}_{01} + \epsilon_d \cos(\omega_d t)$, with a modulation amplitude $\epsilon_d = \epsilon_\Phi \, \partial\omega_{01}/\partial\Phi|_{\Phi_b}$. This flux modulation tone translates to a modulation of the potential at a single site (Q_3) $\epsilon_d n_3 \cos(\omega_d t)$, a tool which we can use for resonantly driving excitations in a many-body system [8]. Matching the flux-drive frequency to the energy required to generate

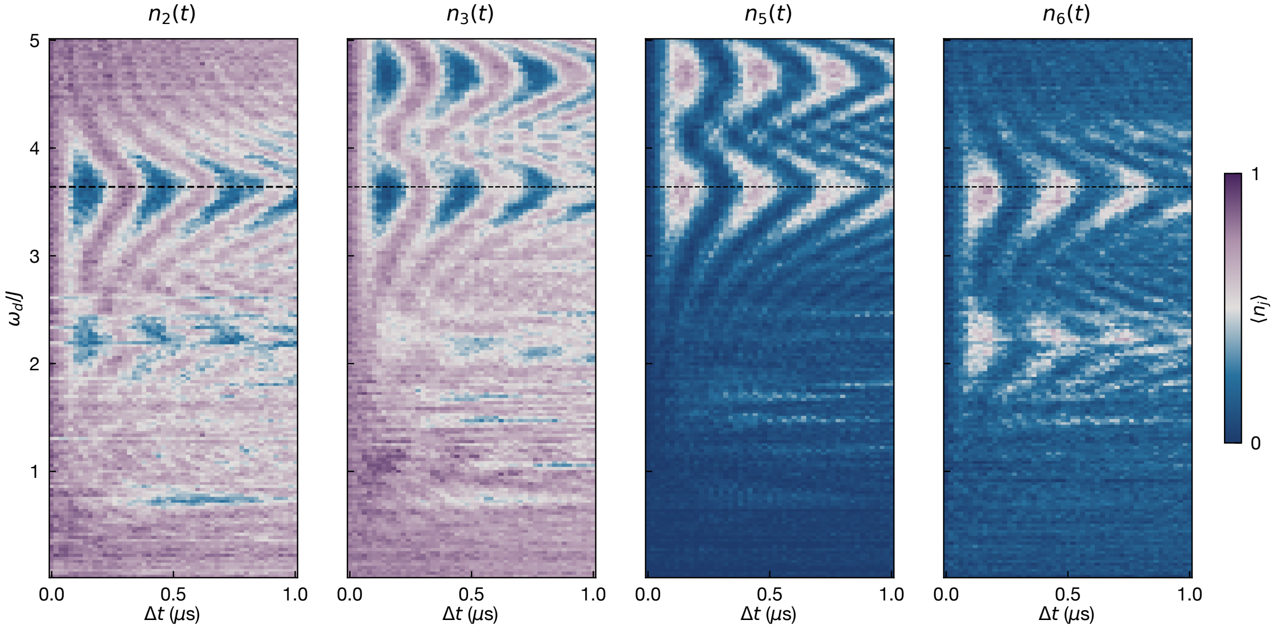

Supplemental Information Fig. S3. **Phonon-induced SWAP operations** in the disordered (computational) qubit basis, where we are varying the flux modulation tone over a wider range of frequencies.

the particle-hole pairs $\omega_d = \varepsilon_4 - \varepsilon_1 = \varepsilon_5 - \varepsilon_2$ leads to coherent Rabi oscillations between the fluid eigenstates $|\Psi_{4,5}\rangle$ and $|\Psi_{1,2}\rangle$ at the edges of the hardcore energy band. This localized lattice perturbation, through the single-site density operator n_3, drives resonant transitions between the two many-body states with an effective Rabi coupling rate proportional to $\propto \langle\Psi_{4,5}|n_3|\Psi_{1,2}\rangle J_1(\frac{\epsilon_d}{2\omega_d})$ [9, 10], where J_1 is the 1st order Bessel function of the first kind.

After applying the flux modulation tone, we adiabatically reintroduce disorder with a reversed flux ramp and monitor the qubit population as a function of the frequency and duration of the flux modulation pulse. In SI Fig. S3 we plot the occupation of the transmon qubits Q_2, Q_3, Q_5 and Q_6 over a wide range of modulation frequencies (normalized in units of the tunneling frequency $J/2\pi$). In Fig. 3, the zoomed in chevron oscillations reveal that flux driving at $\omega_d \approx 3.64\,J$ stimulates the desired two-phonon process that exchanges excitations between the fluid states in the ordered lattice (in the transistor configuration). This Rabi oscillations between the few-body fluid states adiabatically translates to multi-qubit SWAP oscillations between the localized photons in the disordered lattice, where we are simultaneously swap photons between the qubits on the left (Q_2, Q_3) and right (Q_5, Q_6) side of the ancilla qubit. As a side note, in Fig. S3 we can also see that we are exciting particle-hole pairs between the free fermion states $k = 1\,\&\,k = 5$ and $k = 2\,\&\,k = 4$ when we drive at $\omega_d \approx 4.7J$ and $\omega_d \approx 2.2J$, respectively, which leads to swapping photons (in the disordered basis) between the qubit pairs $Q_3\,\&\,Q4$ and $Q_2\,\&\,Q6$, respectively.

As highlighted in the main text, this phonon mediated SWAP operation is conditioned on the state of the ancilla qubit Q_4, as the flux drive generates phonons in the ordered lattice if we prepare a fluid (compressible) state for Q_4 in $|1\rangle$, and has no effect when preparing an insulating (incompressible) state for Q_4 in $|0\rangle$.

Supplement F: N00N state preparation: adiabatic reversibility

In addition to quantifying the quantum coherence of the prepared N00N state from repeated entangling and disentangling operations in the Ramsey sequenced introduced in section V, we also estimate the errors in the adiabatic evolution of our many-body system by trying to reverse the entangling operation to recover the original product state. Similarly to the generalized Ramsey sequence, we amplify the error by applying multiple pairs of entangling (U) and disentangling ($U^\dagger$) operations after initializing the system with localized photons on one side of the ancilla. We quantify the fidelity from the probability of relocalizing the photons to the initial product state after the last disentangling operation. This sequence is highlighted in the diagram in Fig. S4a. We measure how the population of the initially excited lattice sites decays with the total number of applied entangling+disentangling operations, as show in Fig. S4b for the case of the seven qubit N00N state prepared using the inverted disorder protocol. We extract the

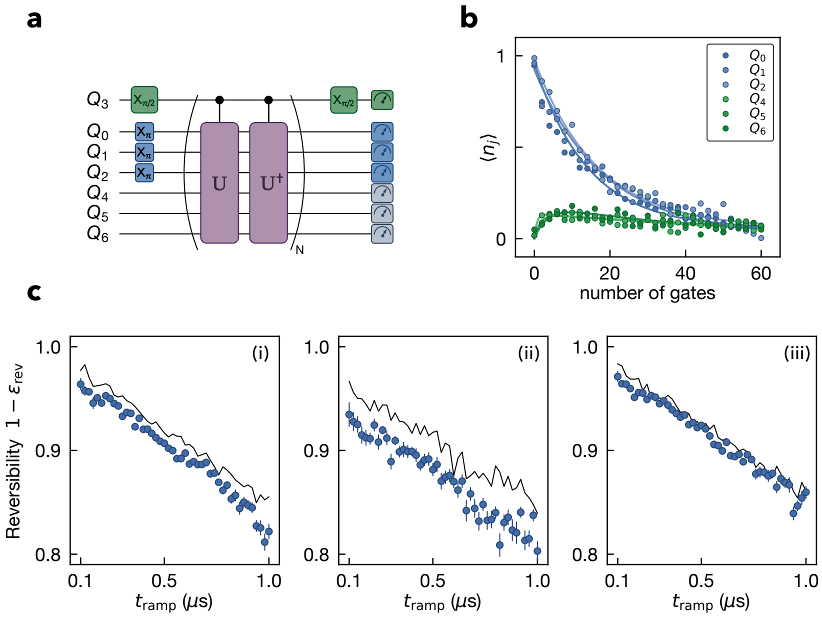

Supplemental Information Fig. S4. **Fidelity of the adiabatic entangling protocol**. **a.** We estimate the fidelity of adiabatically preparing the N00N states by applying multiple pairs of entangling (U) and disentangling ($U^\dagger$) operations. **b.** The average error ϵ_{rev} per entangling/disentanling operation is calculated by probing the occupation of the initially excited qubits and fitting the decay with the number of gates. The dataset corresponds to the seven-qubit N00N state. **c.** The reversibility fidelity $(1-\epsilon_{\mathrm{rev}})$ is measured as a function of the ramp time t_{ramp} for the case of the five-qubit N00N states prepared with the (i) inverted disorder and (ii) phon-assisted protocols, and for the case of the (iii) seven-qubit N00N state prepared with the inverted disorder protocol.

average reversibility error ϵ_{rev} by fitting the decay to $\mathcal{F}_{\mathrm{adb}}(N) = A(1-\epsilon_{\mathrm{rev}})^{2N}$, where N corresponds to the number of $(U^\dagger \cdot U)$ paired operations and we assume they both have the same average error ϵ_{rev} since the same adiabatic ramp trajectories are employed.

In addition to varying the number of applied entangling/disentangling operations, we also vary the ramp time t_{ramp}, over an order of magnitude, and measure the fidelity $(1-\epsilon_{\mathrm{rev}})$ as a function of t_{ramp}. The results for the five- and seven-qubit N00N states are shown in Fig. S4c. For a ramp time of $t_{\mathrm{ramp}} = 240\,\mathrm{ns}$, the measured reversibility error rates are $(5.4 \pm 0.2)\%$ and $(4.7 \pm 0.2)\%$ for preparing the five- and seven-qubit N00N states using the inverted disorder protocol, and $(8.1 \pm 0.3)\%$ for preparing the five-qubit N00N state with the phonon assisted protocol. In the case of the phonon assisted protocol, the measured error rates also include the coherent errors in the SWAP operations attributed to imperfect rotation angles. The measured error rates closely match the decoherence-limited error rates (solid black lines in Fig. S4c), which we measure by setting the ancilla qubit to its ground state $|0\rangle$ (decoupling the entanglement dynamics) and running the same sequence of fast flux pulses on all qubits. This suggests that the error rates are primarily limited by T_1 decay during the adiabatic ramps. The additional errors likely arise from ancilla decoherence and coherent errors in the phonon SWAP operations.

---

[1] Saxberg, B. *et al.* Disorder-assisted assembly of strongly correlated fluids of light. *Nature* **616**, 435–441 (2022).

[2] Roberts, G. *et al.* Manybody interferometry of quantum fluids. *Science Advances* **10**, eado1069 (2024).

[3] Zhao, F. *et al.* Flux-tunable cavity for dark matter detection. *Physical Review Letters* **135**, 201002 (2025).

[4] Blais, A., Grimsmo, A. L., Girvin, S. M. & Wallraff, A. Circuit quantum electrodynamics. *Reviews of Modern Physics* **93**, 025005 (2021).

[5] Ma, R. *et al.* A dissipatively stabilized Mott insulator of photons. *Nature* **566**, 51–57 (2019).

[6] Cazalilla, M. A., Citro, R., Giamarchi, T., Orignac, E. & Rigol, M. One dimensional bosons: From condensed matter systems to ultracold gases. *Reviews of Modern Physics* **83**, 1405–1466 (2011).

[7] Cazalilla, M. A. Differences between the tonks regimes in the continuum and on the lattice. *Phys. Rev. A* **70**, 041604 (2004).

[8] Eckardt, A. Colloquium: Atomic quantum gases in periodically driven optical lattices. *Reviews of Modern Physics* **89**, 011004 (2017).

[9] Vrajitoarea, A., Huang, Z., Groszkowski, P., Koch, J. &

Houck, A. A. Quantum control of an oscillator using a stimulated josephson nonlinearity. *Nature Physics* **16**, 211–217 (2020).

[10] Vrajitoarea, M. A. *Strongly correlated photonic materials: parametric interactions and ultrastrong coupling in circuit QED*. Ph.d. dissertation, Princeton University (2020).